Probing optically driven K_3C_{60} thin films with an ultrafast voltmeter

J. D. Adelinia[1,2†*], E. Wang[1†*], M. Chavez-Cervantes[1], T. Matsuyama[1], M. Fechner[1], M. Buzzi[1], G. Meier[1], A. Cavalleri[1,3*]

[1] *Max Planck Institute for the Structure and Dynamics of Matter, Hamburg, Germany*

[2] *The Hamburg Centre for Ultrafast Imaging, Hamburg, Germany*

[3] *Department of Physics, Clarendon Laboratory, University of Oxford, Oxford, United Kingdom*

[†] *These authors contributed equally to this work*

** Corresponding authors: joseph.adelinia@mpsd.mpg.de, eryin.wang@mpsd.mpg.de, andrea.cavalleri@mpsd.mpg.de*

Supplementary information

Contents

S1. Experimental setup

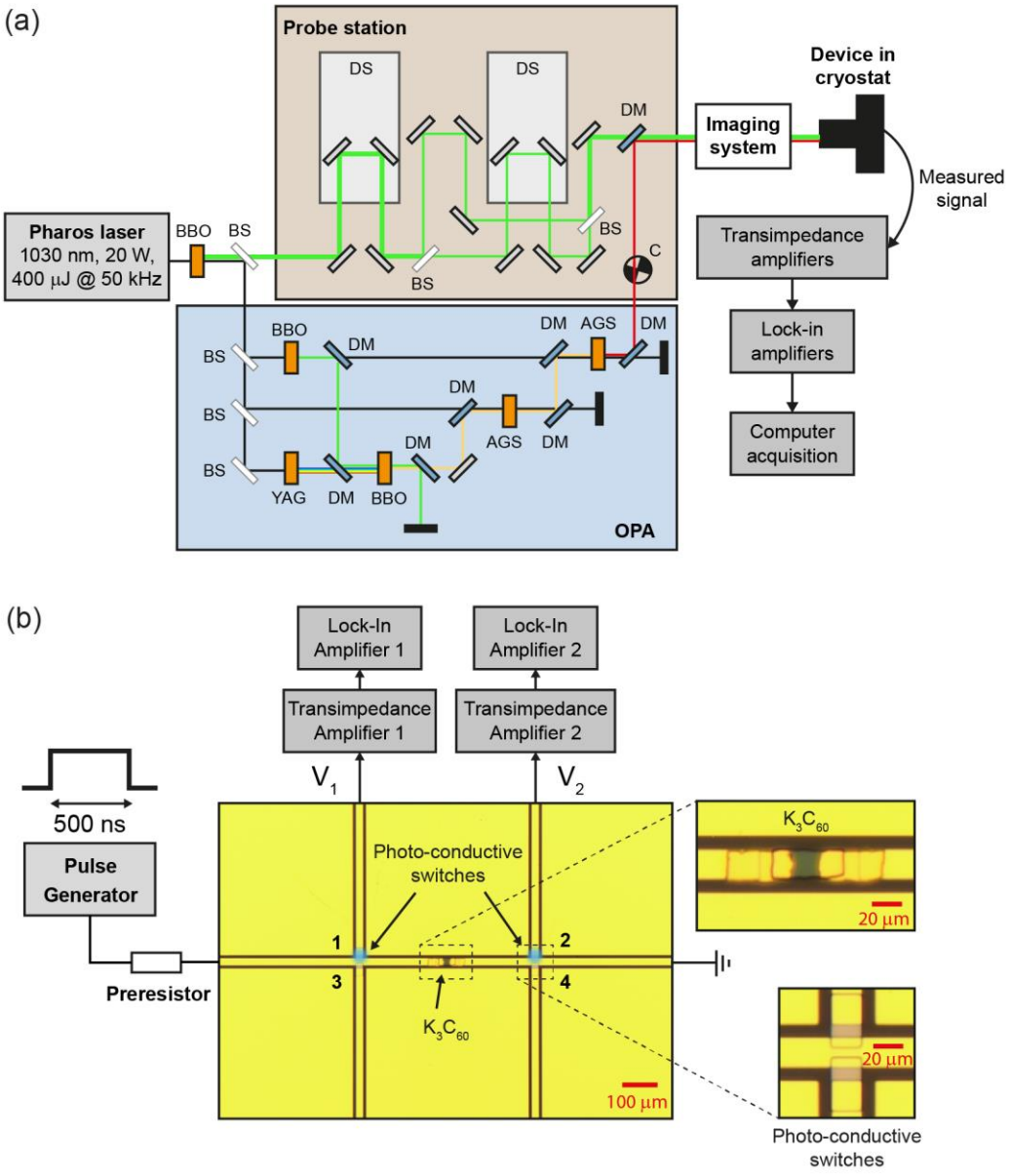

Figure S 1 | Experimental setup. (a), Optical part of the setup. Optical components are abbreviated as follows: AGS – silver thiogallate crystal, BBO – beta barium borate crystal, BS – beam splitter, C – mechanical chopper, DM – dichroic mirror, DS – delay stage, OPA – optical parametric amplifier, YAG – yttrium aluminium garnet. The wavelength of the optical pulses is represented by the colour: 1030 nm (black), 515 nm (green), 1200 nm (yellow), and 7 μm (red). **(b)**, Optical microscope image of the experimental device, showing connections to the external electronics.

A diagram of the experimental setup is displayed in Figure S1. The optical part of the setup is based on a Pharos laser, which outputs pulses of 250-fs duration and 400-μJ pulse energy, with a wavelength centred at 1030 nm, at 50-kHz repetition rate. Part of the pulse energy is converted to 515-nm wavelength via second harmonic generation. This was used to operate the photo-conductive switches. The remainder serves as the input for an optical parametric amplifier (OPA) based on silver thiogallate (AGS)[1], which outputs mid-infrared pulses centred at 7-μm wavelength (43 THz) with 1-THz bandwidth. These were used to excite the K_3C_{60} thin film. The mid-infrared pulses were chopped at a frequency of ~1 kHz. Optical delay lines were used to scan the mutual time delay between the 515-nm pulses and the mid-infrared pulses.

Transient currents in each detection line were sent into in-house custom-built transimpedance amplifiers with a flat frequency dependence, an optimised −3-dB point at 3 kHz, and an amplification factor of $2x10^9$ V/A (the data set at 100 K was acquired with an amplification factor of $2x10^8$ V/A). The voltage output of the transimpedance amplifiers were then sent into lock-in amplifiers, which were trigged at the chopping frequency of the mid-infrared pulses. Data from the lock-in amplifier was acquired digitally using custom software written in LabVIEW.

The characterisation of the mid-infrared pulses, as well as the device fabrication process is discussed in Wang, *et al.* [2].

S2. Device and sample characterisation

S2.1. Determination of the quasi-DC current

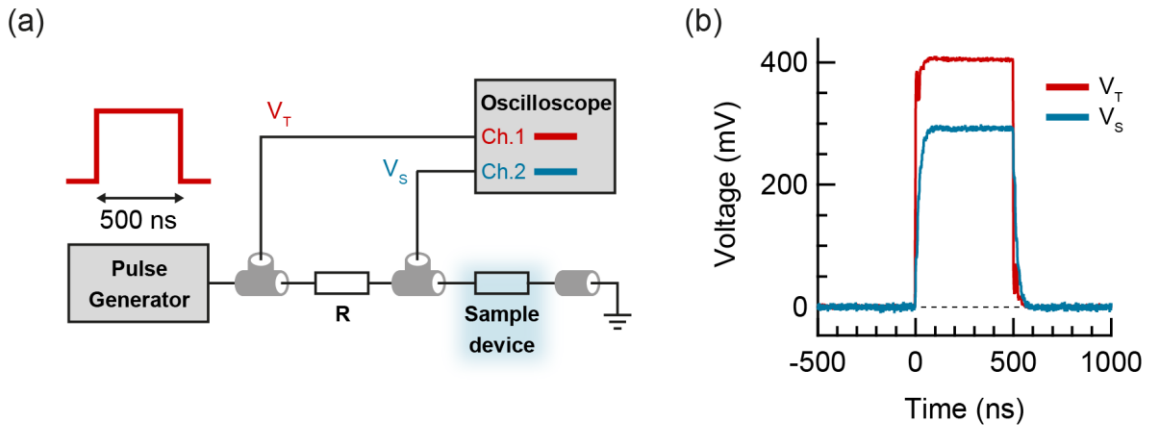

Figure S 2 | Measurement of the applied current. (a), Measurement setup with a pulsed electrical bias of 500-ns duration. **(b)**, Voltage drop across the sample / device under test ($\boldsymbol{V_S}$) and sample + resistor ($\boldsymbol{V_T}$) as a function of time for a 400-mV applied bias.

A quasi-DC current was applied to the K_3C_{60} sample prior to photo-excitation. Flat-top voltage pulses of 500-ns duration were used for this in order to minimise current-induced heating of the sample. To determine the current flowing through the sample when the voltage pulse was present, the setup depicted in Figure S2a was used. A known resistance R was connected in series between the voltage pulse generator and the sample device via coaxial cables. For measurements below and above T_c, resistances of 300 Ω and 100 Ω were used, respectively. The voltages before the resistor V_T and before the sample device V_S relative to ground were monitored using an oscilloscope. An example measurement for a pulsed bias of 400 mV is displayed in Figure S2b. The stabilised voltage values could be read out at a time of 300 ns. The current flow I in the device was then obtained from the equation $I = (V_T - V_S)/R$.

S2.2. Waveguide characterisation

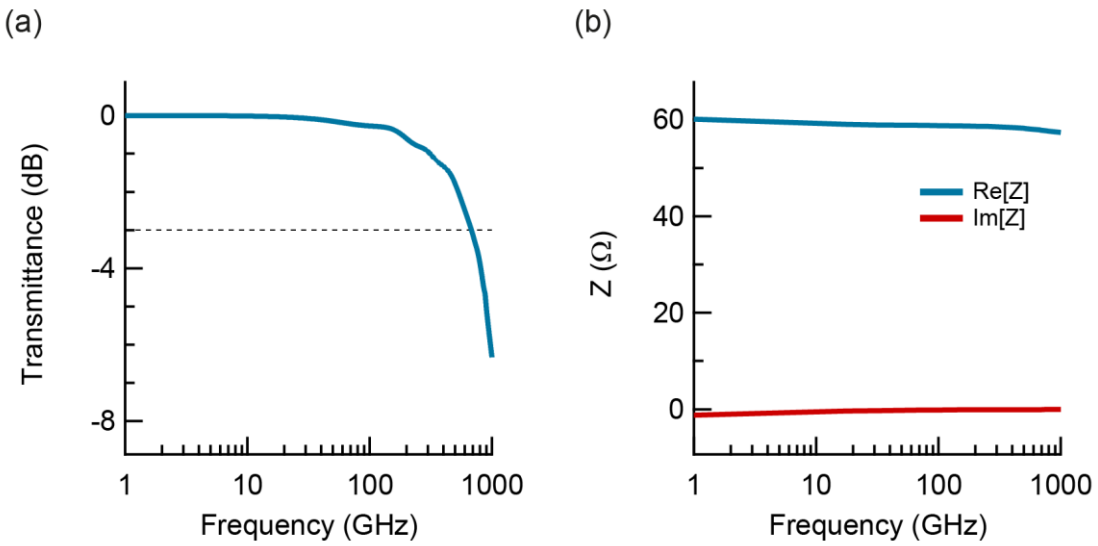

Figure S 3 | Waveguide characterisation. (a), Simulated transmittance versus frequency of a 200-μm long section of a gold coplanar waveguide with the same dimensions as used in the device. **(b)**, Real and imaginary components of the wave impedance versus frequency. [2]

Another important factor affecting the time resolution of the experiment is the dispersion in the coplanar waveguide. To determine the impact of this, the frequency-dependent transmittance in a 200-μm long waveguide was simulated in CST studio suite. The result is shown in Figure S3a. The transmittance drops off sharply at high frequencies, with the −3-dB point at approximately 700 GHz.

The simulated frequency-dependent complex impedance from Wang, *et al*. [2] is shown in Figure S3b. Both real and imaginary components display little variation within the experimental bandwidth. The real component Re[Z] is approximately 59 Ω, while the imaginary component Im[Z] is < 0.2 Ω and is therefore negligible.

S2.3. K_3C_{60} thin film characterisation

A line profile from an AFM micrograph of the C_{60} film edge is displayed in Figure S4, showing a film thickness of approximately 100 nm.

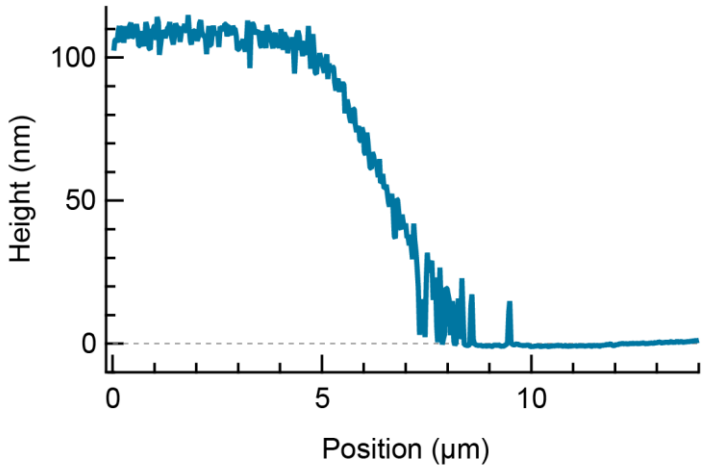

Figure S 4 | Edge of the K_3C_{60} thin film. Line cut of an AFM micrograph of the sample.

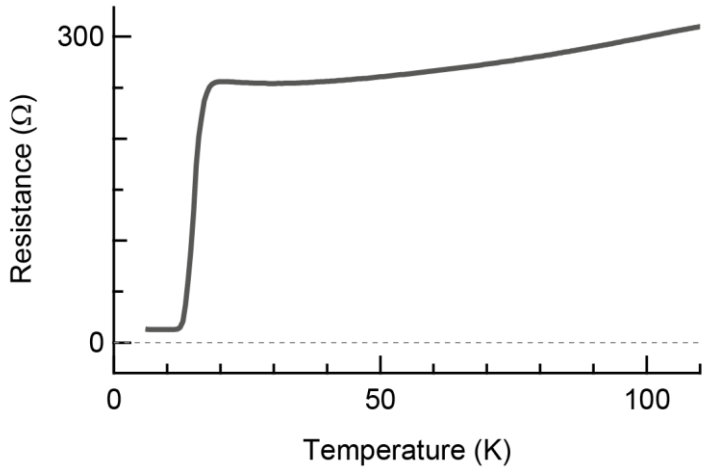

Figure S 5 | Resistance vs temperature of the K_3C_{60} thin film. Measured in a two-contact configuration under a DC current bias of 1 μA. [2]

The resistance vs temperature of the K_3C_{60} thin film, as measured in a two-contact geometry in the device used for the pump-probe experiment, is displayed in Figure S5. The measurement displays a decrease in the sample resistance with decreasing temperature, consistent with the metallic behaviour indicated by previous studies[3,4]. The measurement was carried out with a DC current bias of 1 μA.

S3. Raw data and data analysis

Figures S6, S7, S8, and S9 display the raw signal at the lock-in amplifier for each measurement. In this section, we describe the complete data analysis pipeline, which consisted of the following steps:

i. Subtraction of the signal at zero current.
ii. Subtraction of the offset before time-zero.
iii. Subtraction of reflections.
iv. Calibration of the on-chip voltage changes.
v. Normalisation of voltage changes.

The first step in analysis was to subtract the data obtained with 0 mA bias from the data at finite bias. This is necessary because the mid-infrared pulse has finite intensity in the gap between the K_3C_{60} thin film and the waveguide, and the excitation pulse can couple into the waveguide and induce an electrical signal that is not related to the carrier dynamics in the K_3C_{60} and distort the data at finite bias. For most of the measurements, the signal at 0 mA bias was nevertheless negligibly small.

For the second step, we subtract the signal offset before time-zero. Importantly, we are sure that this offset is not a long-lived response from the pump. First, we consider Figure S10a, which displays an oscilloscope measurement of the voltage across the device under test *with* high-fluence mid-infrared excitation. After the pump pulse arrives at a time of ~300 ns, the voltage drop across the device increases sharply, but almost completely recovers before the end of the voltage pulse, and the following excitation pulse will not arrive for another 20 µs. Second, the offset is consistently ~12 % of the signal magnitude – an example for the 8 K data is shown in Figure S10b – independent of the sign of the response. This suggests that the offset arises from leakage currents at the photoconductive switches, which result in a constant voltage at the lock-in amplifier that is proportional to the time-integral of the photo-induced voltage changes.

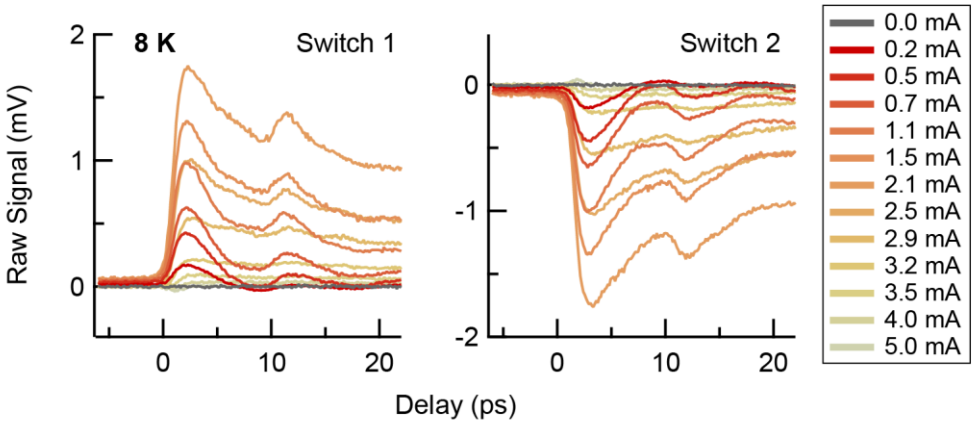

Figure S 6 | Raw low-fluence data at 8 K. Measured with < 100 μJ/cm². Even without subtraction of reflections, a bipolar response is seen for the smallest currents.

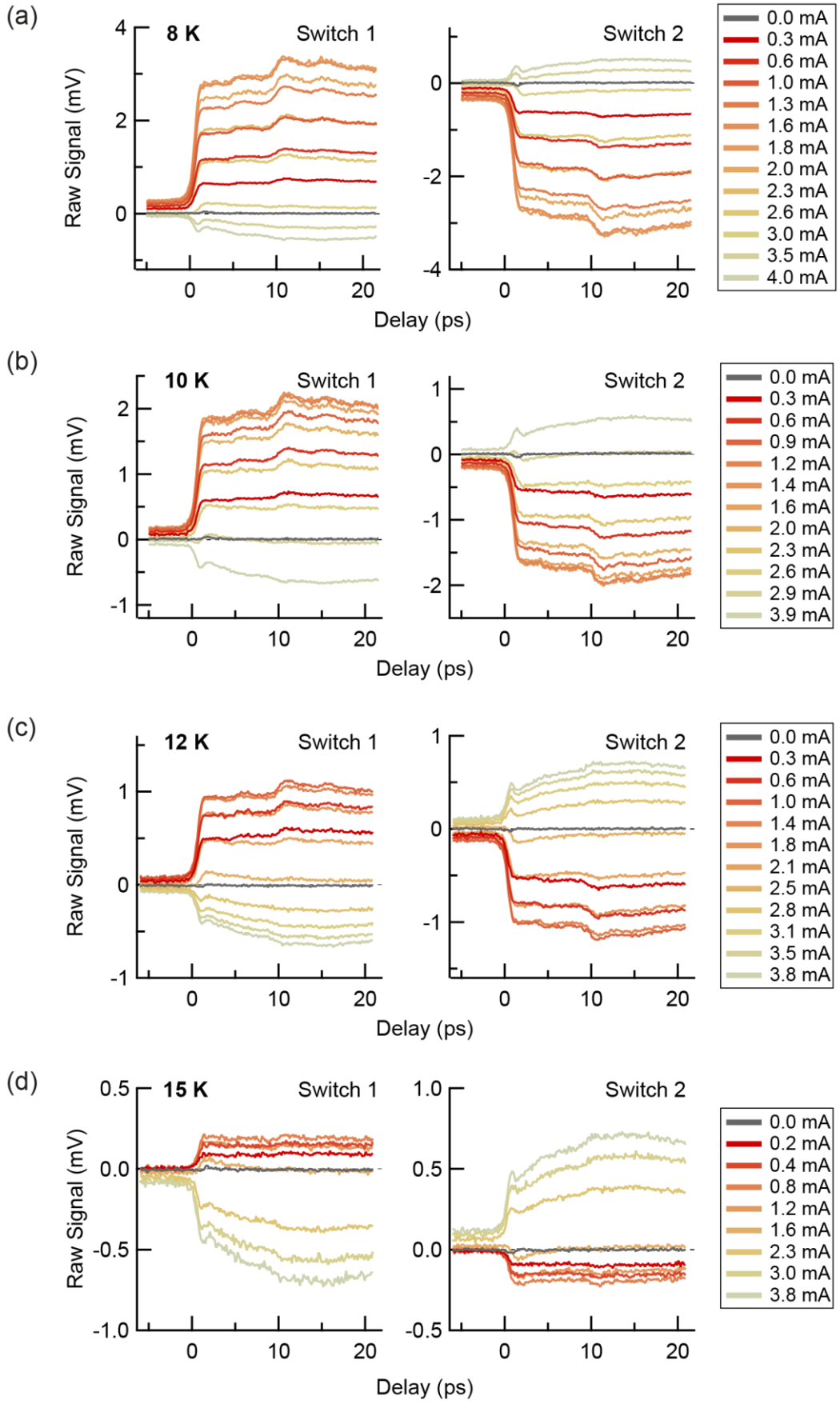

Figure S 7 | Raw data at temperatures below T_c. Measured at **(a)** 8 K, **(b)** 10 K, **(c)** 12 K, and **(d)** 15 K with a fluence of 5 mJ/cm^2.

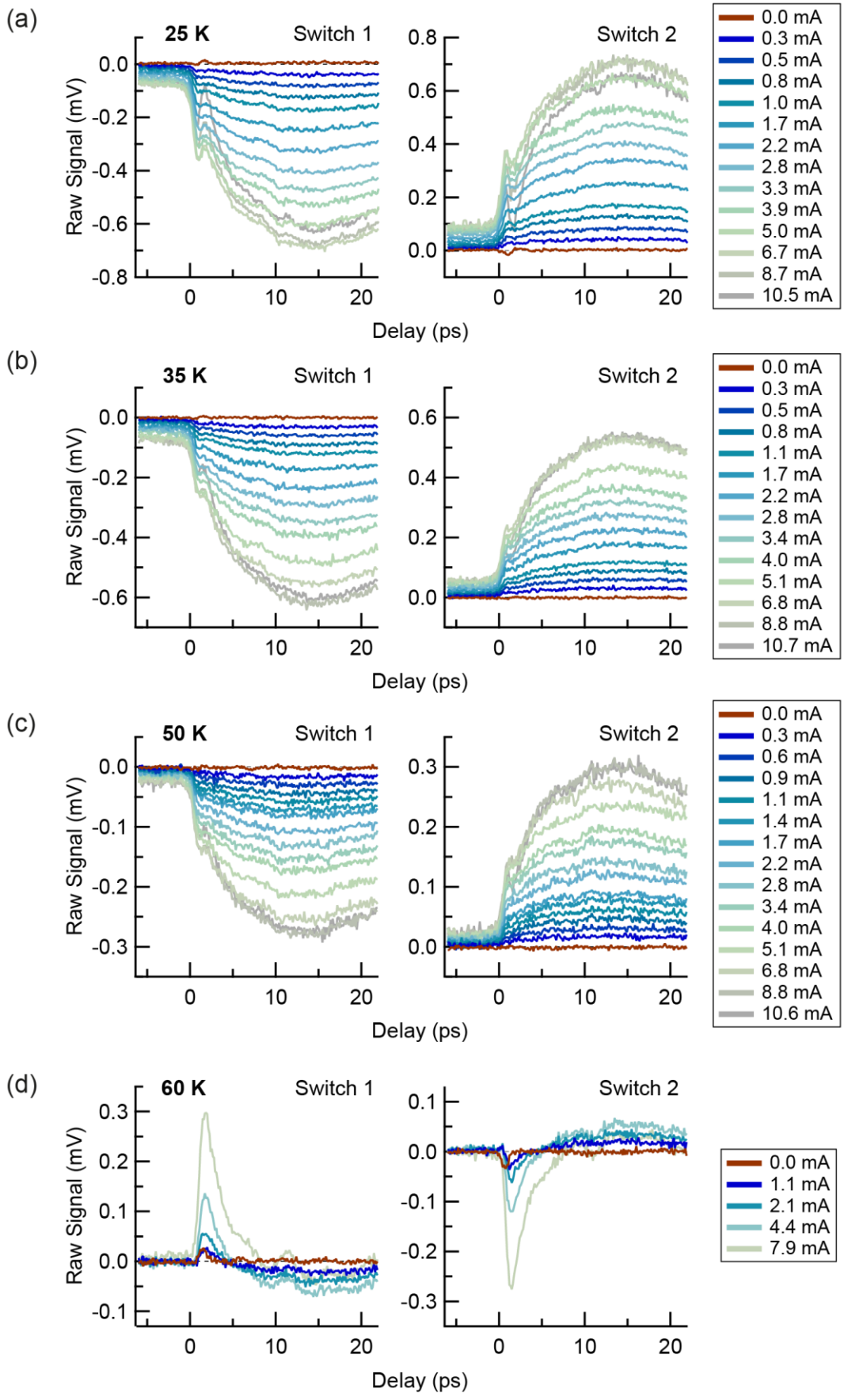

Figure S 8 | Raw data at temperatures above T_c. Measured at **(a)** 25 K, **(b)** 35 K, **(c)** 50 K, and **(d)** 60 K with a fluence of 5 mJ/cm^2.

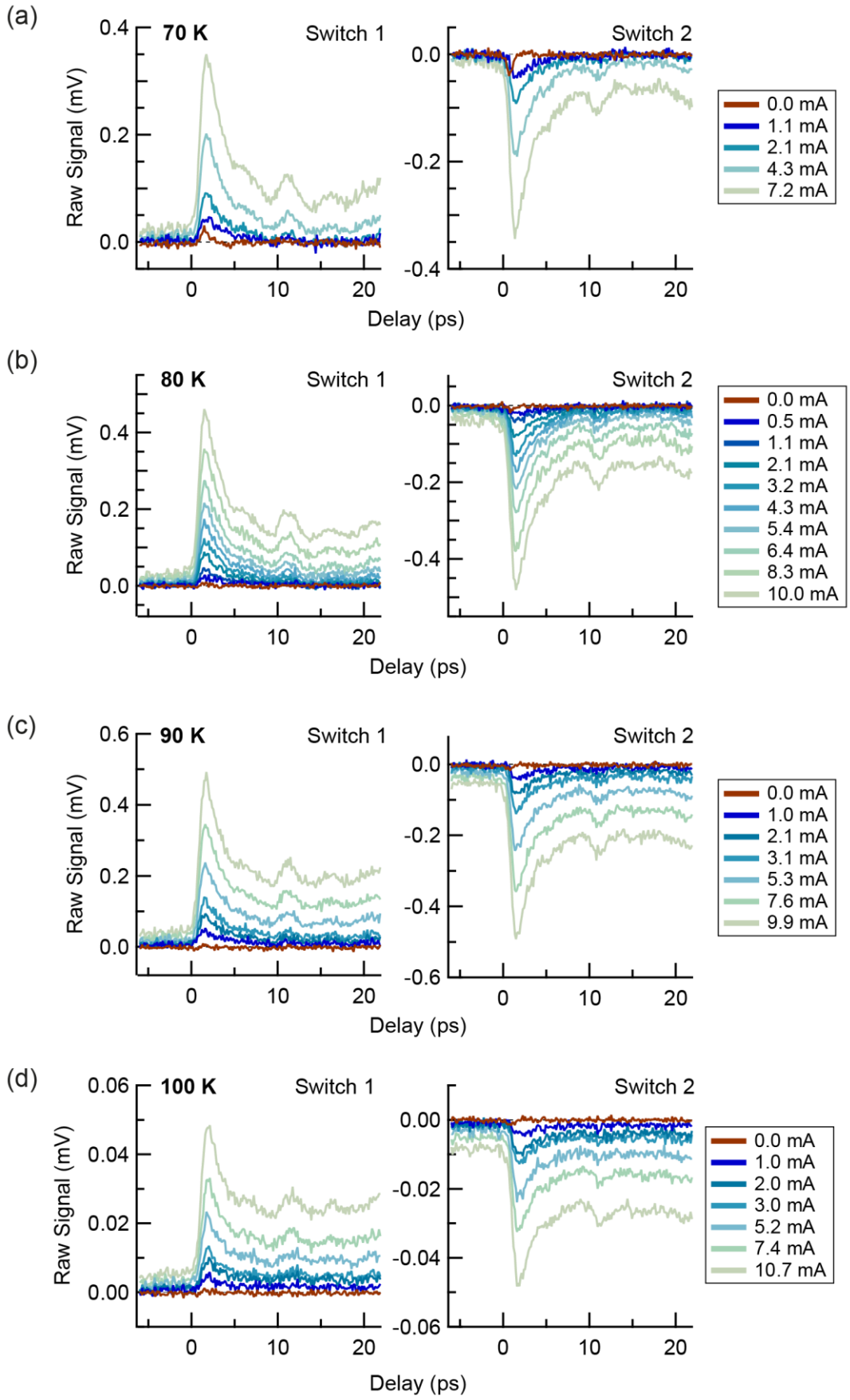

Figure S 9 | Raw data at temperatures above T_c (continued). Measured at **(a)** 70 K, **(b)** 80 K, **(c)** 90 K, and **(d)** 100 K with a fluence of 5 mJ/cm^2.

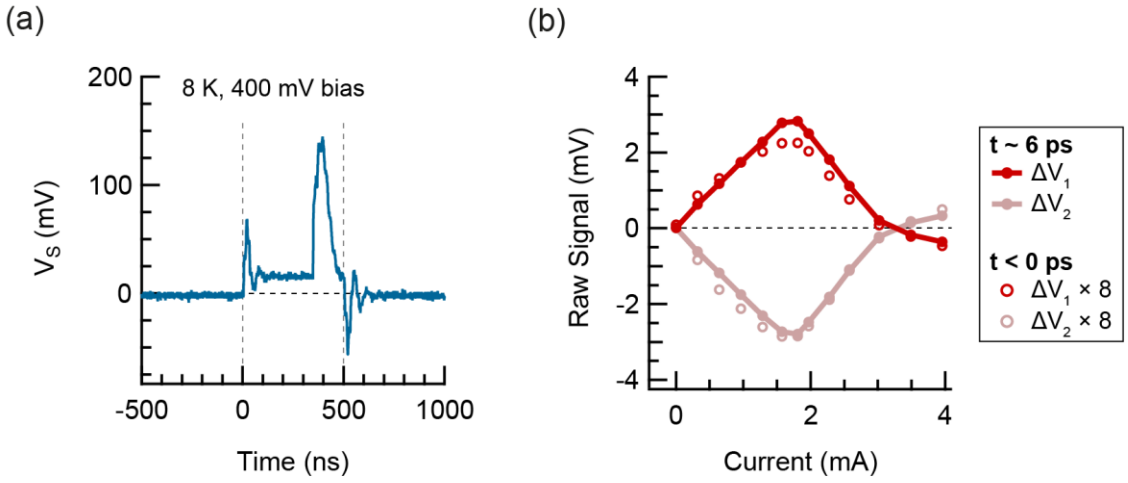

Figure S 10 | Determining the origin of the offset. (a), Oscilloscope trace of the voltage across the device (as in Fig. S2) at 8 K. The vertical dashed lines mark the start and end of the externally-applied voltage pulse. The mid-infrared pump arrives at a time of ~ 300 ns. **(b)**, Transient voltage changes at 8 K (filled circles), and the offset before 0 ps delay (open circles).

For the third step, we consider reflections from the photo-conductive switches. A zoomed-out optical microscope image of the device geometry is displayed in Figure S11a. Additional pairs of photo-conductive switches can be seen on the left and right sides of the image. In the experiment, a voltage pulse originated at the K_3C_{60} thin film (image centre) and propagated outwards along the waveguide towards the detection switches 1 and 2. Without loss of generality for the discussion of reflections, we will consider the leftward propagating pulse. At switch 1, the pulse is partially reflected back towards the sample and partially transmitted. The reflected pulse is again reflected from the sample and returns to switch 1 (green arrow), while the transmitted pulse is reflected from the leftmost pair of switches (blue arrow) and returns to switch 1 at a later time.

The arrival time of the reflected pulses can be estimated as follows. We consider the distance d_1 between switch 1 and the K_3C_{60} thin film, the distance d_2 between switch 1 and the leftmost pair of switches, and the effective relative dielectric constant of the coplanar waveguide on the sapphire substrate. We have $d_1 = 280$ µm and $d_2 = 600$ µm. For the effective relative dielectric constant, $\epsilon_r = (\epsilon_{Al_2O_3} + 1)/2 = 5.27$, giving a pulse propagation speed $v = 0.43c$, where c is the speed of light in vacuum. The arrival times t_n for the reflections can be calculated as

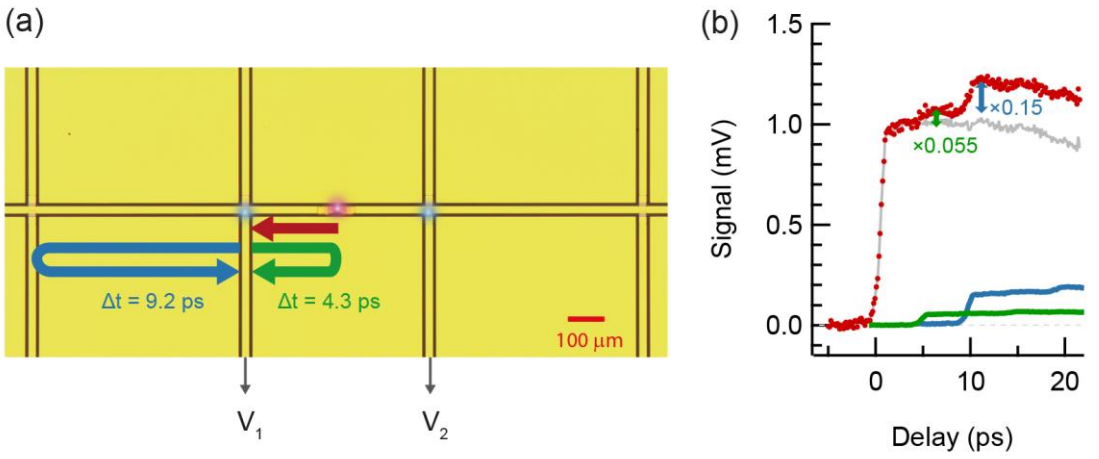

Figure S 11 | Subtraction of reflections. (a), A zoomed-out microscope image of the device. The transient voltage changes propagate towards the detection switches (red arrow), after which reflections from the sample (green arrow) and from an additional pair of switches (blue arrow) occur with time offsets $\boldsymbol{\Delta t}$ of 4.3 ps and 9.2 ps, respectively. **(b)**, Illustration of the reflection removal procedure. An example data set at 8 K and 0.6 mA after subtraction of the zero-bias signal and voltage offset is displayed in red. The same measurement, offset in time by 4.3 ps (9.2 ps) and scaled by a factor 0.055 (0.15), is shown in green (blue). The green and blue traces are subtracted from the red trace to obtain the processed signal, shown in grey.

$$t_n = \frac{2d_n}{v}, \tag{3.1}$$

giving 4.3 ps and 9.2 ps for the distances d_1 and d_2, respectively.

Figure S11b shows data measured at 8 K with a 0.6 mA current after subtracting the offset and zero-bias signal (red data points). Clear steps can be seen at ~4 ps and ~9 ps, as expected. To remove the reflections in a first-order approximation, copies of the data were scaled to 0.055 and 0.15 and offset in time by 4.3 ps and 9.2 ps, respectively, as shown in green and blue. The processed signal (grey) was obtained by subtracting these traces from the data. This process was repeated identically for every measurement using the same parameters.

The data after processing are displayed in Figures S12, S13, S14, and S15, with the left axis (black) representing the signal magnitude at this stage in the process, before calibration.

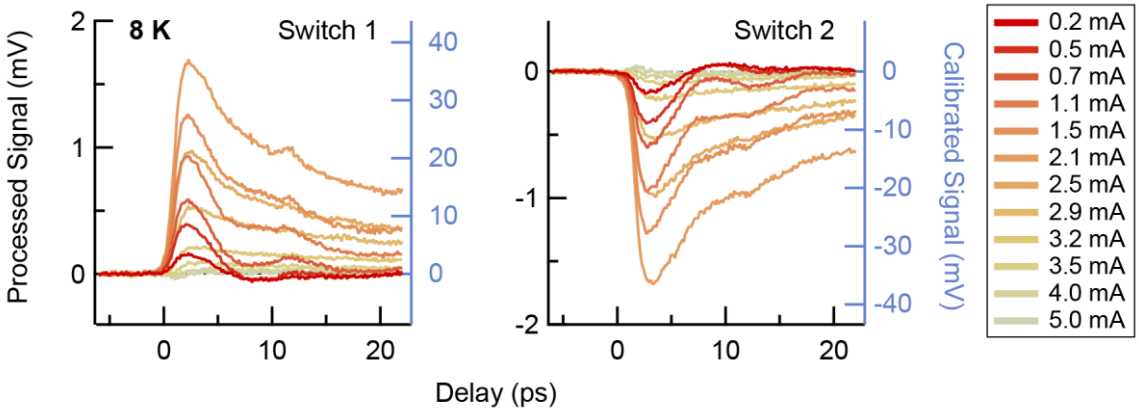

Figure S 12 | Processed low-fluence data at 8 K. Data is shown for a fluence of < 100 µJ/cm^2. The data is displayed after subtraction of before-time-zero offset, 0 mV signal, and reflections at 4.3 ps and 9.2 ps. The blue axis represents the calibrated voltages.

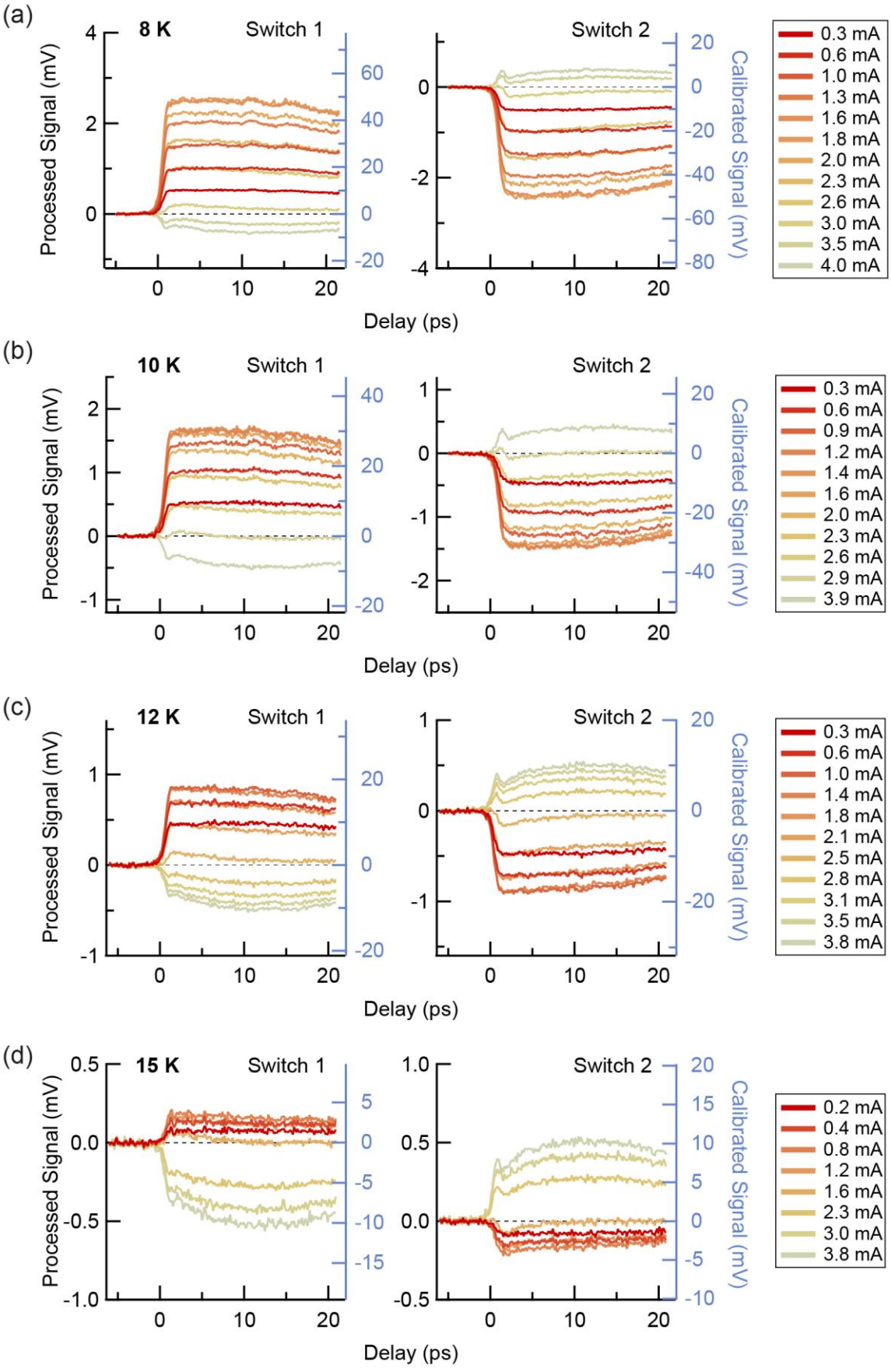

Figure S 13 | Processed data at temperatures below T_c. Data is shown for **(a)** 8 K, **(b)** 10 K, **(c)** 12 K, and (d) 15 K with a fluence of 5 mJ/cm^2. The data is displayed after subtraction of before-time-zero offset, 0 mV signal, and reflections at 4.3 ps and 9.2 ps. The blue axis represents the calibrated voltages.

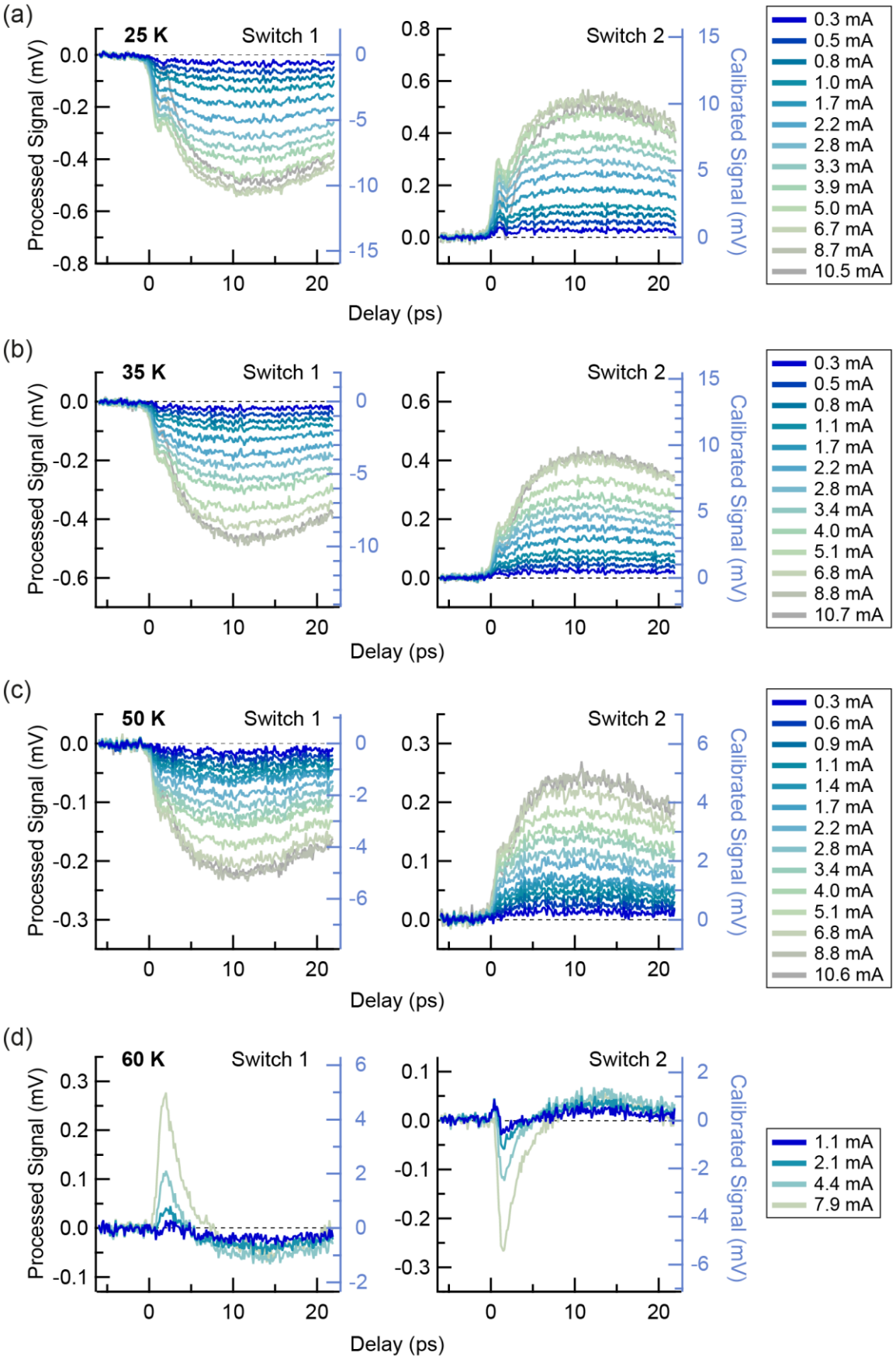

Figure S 14 | Processed data at temperatures above T_c. Data is shown for **(a)** 25 K, **(b)** 35 K, **(c)** 50 K, and **(d)** 60 K with a fluence of 5 mJ/cm^2. The data is displayed after subtraction of before-time-zero offset, 0 mV signal, and reflections at 4.3 ps and 9.2 ps. The blue axis represents the calibrated voltages.

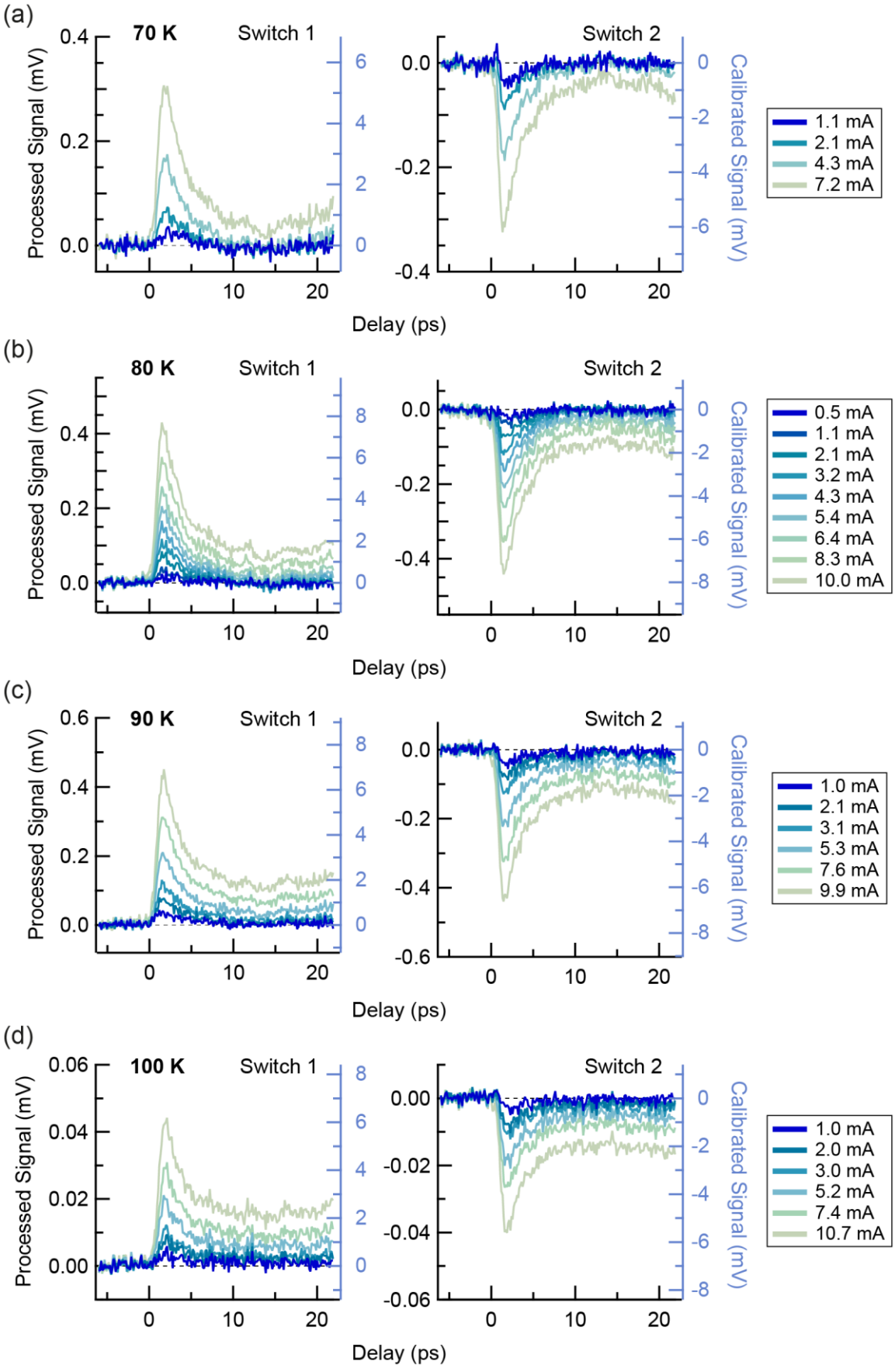

Figure S 15 | Processed data at temperatures above T_c. Data is shown for **(a)** 70 K, **(b)** 80 K, **(c)** 90 K, and (d) 100 K with a fluence of 5 mJ/cm². The data is displayed after subtraction of before-time-zero offset, 0 mV signal, and reflections at 4.3 ps and 9.2 ps. The blue axis represents the calibrated voltages.

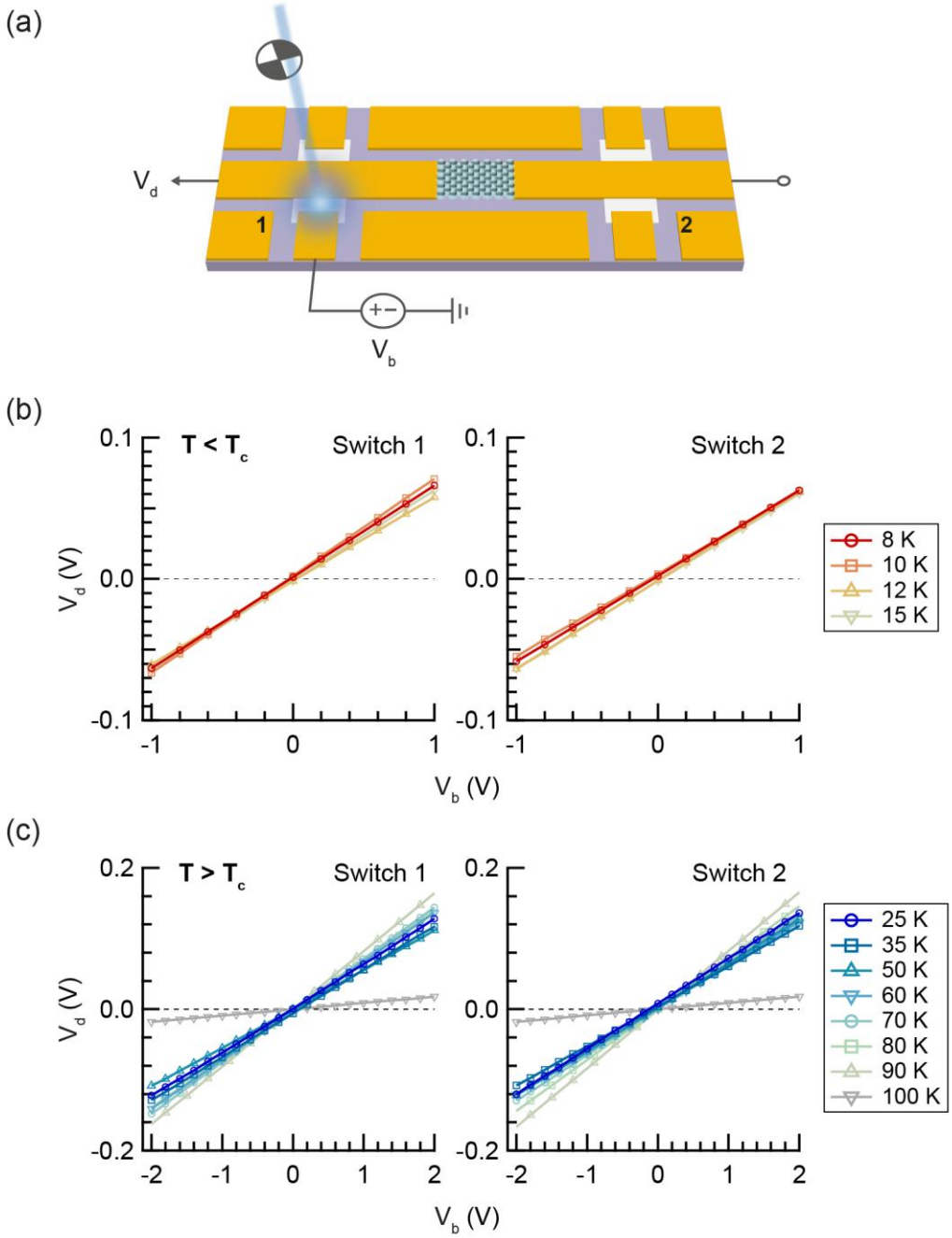

Figure S 16 | Calibration curves. (a), Configuration for the calibration measurements. Also shown is the measured output voltage $\boldsymbol{V_d}$ of the photo-conductive switches when photo-excited under a DC voltage bias $\boldsymbol{V_b}$ for temperatures **(b)** below T_c and **(c)** above T_c. The amplifier configuration was the same as that used in the time-resolved measurements. The gradient of these curves was used to retrieve the voltage in the waveguide from the measured raw signal. At 100 K, a transimpedance amplifier with a smaller amplification factor of 2×10^8 V/A was used to prevent lock-in amplifier overload due to dark currents, resulting in the smaller signal.

The calibrated voltages are shown on the right axis (blue), and were obtained using a calibration procedure similar to the one described in McIver, *et al.* [5]. The calibration measurements are shown in Figure S16. A DC voltage bias V_b was applied to the photo-conductive switch. The switch was illuminated with laser pulses at 515-nm wavelength, which were chopped at a frequency of ~1 kHz. Upon illumination, a voltage V_d was detected using the same amplification chain as in the experiment. Figure S16b and c display V_d versus V_b for switches 1 and 2 at temperatures below and above T_c. The switch response was linear for all temperatures. From the gradient of these curves, we obtain a calibration factor κ_S, defined by $V_b/V_d = 1/\kappa_S$, that relates the measured voltage at switch S to the voltage present in the waveguide.

However, directly using the κ_S obtained from this measurement is expected to underestimate the magnitude of the voltage changes for two reasons. First, a travelling voltage pulse in the coplanar waveguide will be partially reflected from the photo-conductive switch. This occurs because the switch influences the local transmission line impedance, and can be quantitatively accounted for by considering the transmittance of the switch. With the detected reflections discussed previously, we see that the second reflection of 15 % magnitude (blue arrow in Figure S11a) involves the transmission from one pair of switches and the reflection from the other pair. It follows that the switch transmittance T for the transient voltages in the experiment can be estimated using $T(1-T) = 0.15$. This gives $T \approx 0.8$. We can therefore account for reflections by scaling the calibration factor obtained previously by $\kappa_S \rightarrow \kappa_S/0.8 = 1.25\kappa_S$.

Second, the laser pulses incident on the switch will result in heating and an increase in DC conductivity, leading to a leakage current. This effect will last as long as the thermal dissipation time of several tens of nanoseconds. The leakage current therefore provides an additional contribution to V_d in the calibration measurement. This means that the detected voltage with a DC bias is larger than with a several-picosecond voltage bias of the same magnitude. We cannot easily account for this quantitatively, so our calibration method uses a factor of $1.25\kappa_S$, and a systematic uncertainty exists in the magnitude of the voltage changes.

By multiplying the processed data in Figures S12, S13, S14, and S15 by $1.25\kappa_S$, we obtain the calibrated voltages on the right (blue) axes of the respective plots. The ultrafast voltmeter data from the K_3C_{60} thin film at 8 K, calibrated using this factor (grey data points), is displayed in Figure S17 alongside the simulated voltage changes for disruption

of superconductivity (red line). The quantitative discrepancy is consistent with a small underestimation of the on-chip voltage changes due to leakage current in the calibration measurement.

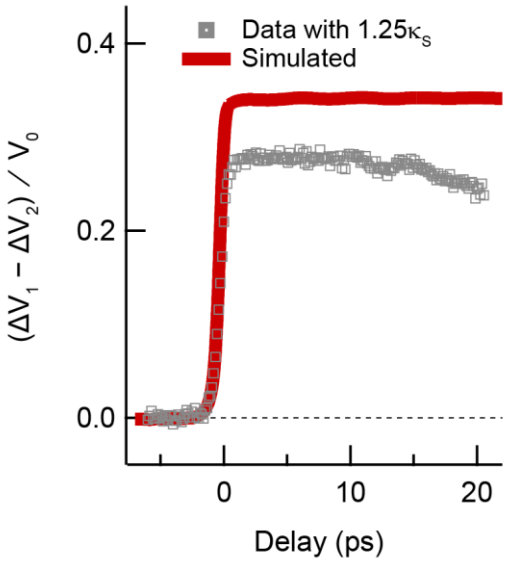

Figure S 17 | Comparison of calibrated data with simulation. Transient voltage changes at 8 K with a 0.3 mA bias, calibrated using a factor of $\mathbf{1.25}\boldsymbol{\kappa_S}$, alongside the simulated voltage changes for disruption of superconductivity.

Finally, as described in the main text, the total change in voltage drop was obtained as $\Delta V_1 - \Delta V_2$, and voltages were normalised by the equilibrium voltage drop across the sample for the measurements above T_c, and by the voltage drop across the sample in its metallic state (taken to be 230 Ω) for the measurements below T_c. The former was estimated by subtracting the 13 Ω residual resistance from the measured equilibrium resistance data (Figure S18), and multiplying by the applied current for each measurement.

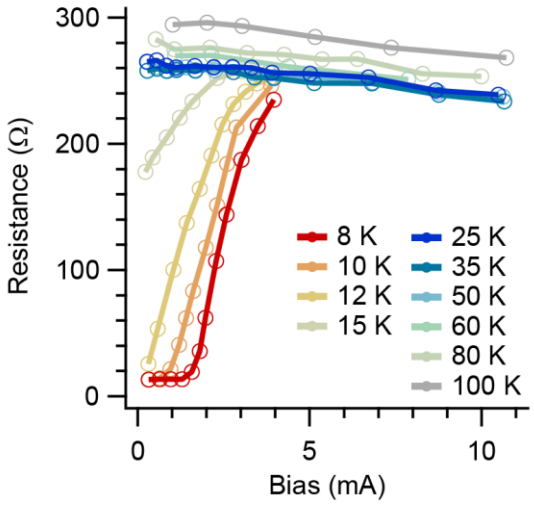

Figure S 18 | Resistance versus current. Measured in a two-contact geometry under a quasi-DC voltage bias.

S4. Voltage dynamics simulation

S4.1. Voltage due to kinetic inductance for time-dependent carrier densities

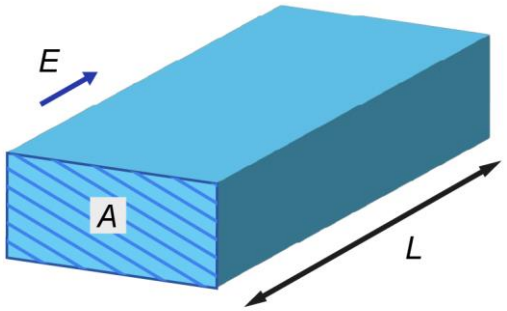

Figure S 19 | Definitions for kinetic inductance derivation.

Kinetic inductance is an inductive electronic behaviour that arises due to the inertia of the charge carriers [6]. A simplified way to understand this behaviour in a conductor is to consider the equations of motion for charge carriers in an electric field. We consider a material of length L and cross-sectional area A, with an electric field E applied along the direction of L, as illustrated in Figure S19. For a charge carrier with charge e and mass m_e, the equation of motion for the velocity v is given by

$$\frac{dv}{dt} = -\frac{eE}{m}, \tag{4.1}$$

where we neglect the scattering term for this treatment. Assuming, for now, that the charge carrier density n is constant, the current density J can then be calculated as

$$\frac{dJ}{dt} = \frac{ne^2}{m_e}E. \tag{4.2}$$

We now make use of the material geometry to extract a voltage-current relation, under the assumption of a spatially uniform electric field. This gives

$$V = \left(\frac{m_e}{ne^2}\right)\left(\frac{L}{A}\right)\frac{dI}{dt}, \tag{4.3}$$

which displays equivalent behaviour to an inductor, and can be written as

$$V = L_K \frac{dI}{dt}, \tag{4.4}$$

where the kinetic inductance is therefore defined as

$$L_K = \left(\frac{m_e}{ne^2}\right)\left(\frac{L}{A}\right). \tag{4.5}$$

For a time-dependent carrier density, the current density is instead given by

$$\frac{d}{dt}\left(\frac{J}{n}\right) = \frac{e^2}{m_e}E, \tag{4.6}$$

and the voltage-current relation becomes

$$V = L_K \frac{dI}{dt} + I\frac{dL_K}{dt}. \tag{4.7}$$

S4.2. Estimation of heating due to the pump pulse

In a granular superconductor, the onset of resistivity at temperatures just below T_c is understood to result from thermal fluctuations in the phase of the order parameter, which disrupt Josephson tunnelling across the grain boundaries [7,8]. In order to consider the role this plays in the photo-induced superconducting-like state, the thermal fluctuations were estimated by accounting for the heating effect of the mid-infrared pump pulse.

First, the absorbed fraction of the mid-infrared pulse energy was estimated to be 30 % of the incident energy using a 3-layer multireflection model, where the optical properties were taken from Degiorgi, *et al*. [3]. The absorbed energy E_{Abs} is therefore given by $E_{Abs} = 0.3 \times Fluence \times Sample\ Area$. To calculate the incident power, a Gaussian laser pulse with a full-width-half-maximum of 300 fs was scaled such that its integral was equal to E_{Abs}, as displayed in Figure S20a.

To calculate the increase in carrier and lattice temperature in the K_3C_{60} thin film, we used a two-temperature model with the following form [9,10]

$$c_e \frac{dT_e}{dt} = -\frac{c_e}{\tau_{e-p}}\left(T_e - T_p\right) + P(t) \tag{4.8}$$

$$c_p \frac{dT_p}{dt} = \frac{c_e}{\tau_{e-p}}(T_e - T_p) - \frac{c_p}{\tau_{es}}(T_p - T_0), \tag{4.9}$$

where T_e and T_p are the electron and phonon temperatures, respectively, c_e and c_p are the electron and phonon specific heat capacity, τ_{e-p} is approximately the electron-phonon scattering time, and τ_{es} is the "escape time", representing the rate of heat transfer from the thin film to the substrate.

For films of tens of nanometres in thickness, the escape time τ_{es} is on the order of tens of nanoseconds and is not important on the timescales of this experiment [9]. A value of 3 ns was used here. Measurements in other metals have found values for the electron-phonon relaxation time τ_{e-p} of ~1 ps. In the simulations reported here, $\tau_{e-p} = 0.8$ ps provided the best fit to the data.

The value of the phononic specific heat capacity was obtained from fits to calorimetry data[11], where $c_p(T)$ was approximated as linear within the range of 0 – 300 K. For the electronic specific heat capacity $c_e(T) = \gamma T_e$, a value of $\gamma = 3.7 \times 10^{-2}$ J/kg K^2 was used.

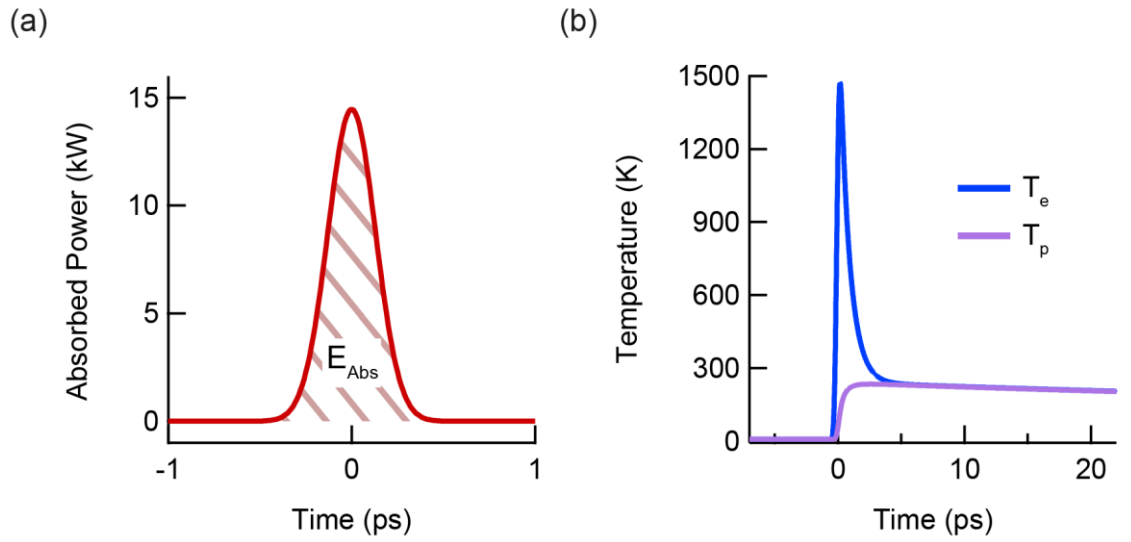

Figure S 20 | Estimation of pump-induced heating. (a), Absorbed power for a Gaussian pulse with a fluence of 5 mJ/cm^2. **(b)**, Calculated electron temperature ($\boldsymbol{T_e}$) and lattice temperature ($\boldsymbol{T_p}$) vs time for photo-excitation of K_3C_{60} with the Gaussian pulse shown in (a).

The calculated T_e and T_p for a 5-mJ/cm^2 excitation fluence are displayed in Figure S20b. The electron temperature rises sharply during the excitation, and the lattice temperature increases on longer timescales due to electron-phonon scattering, with the electron and

lattice temperatures stabilising at ~300 K after several picoseconds. The thermal phase fluctuations in the granular two-fluid model simulation were assumed to follow the electron temperature calculated here.

S4.3. Simple two-fluid model

The full circuit model used for the simple two-fluid model simulation is displayed in Figure S21. The two-fluid model, highlighted in red, was biased with a DC current. In the experiment, the transient voltage changes were detected at the photo-conductive switch positions after propagating along the coplanar waveguide, indicated by the high pass filter symbols, which had a wave impedance of Z_W. To separate the transient voltage changes in the simulation, the DC bias was isolated via low-pass filters, also indicated in Figure S21.

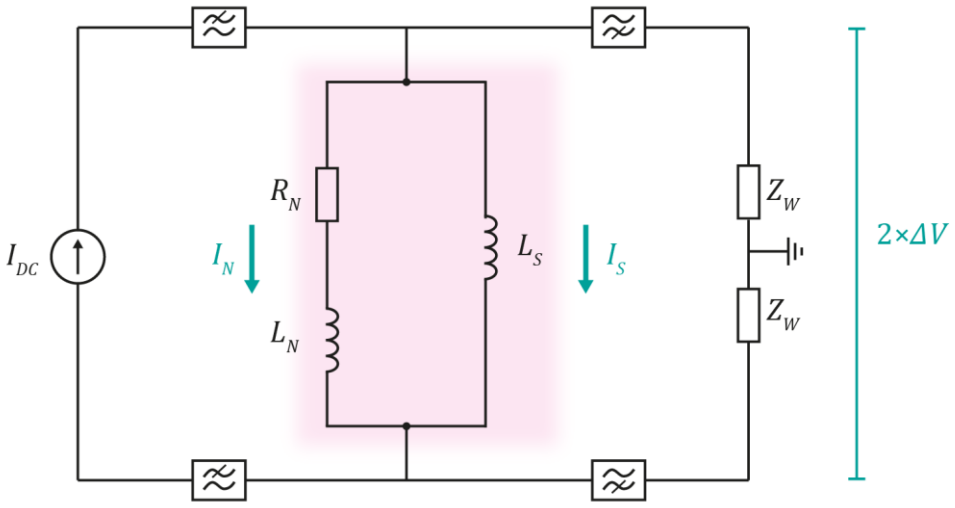

Figure S 21 | Full circuit model for simple two-fluid model simulations. The model for the sample is highlighted in red. The right part of the circuit represents the impedance of the coplanar waveguide.

Determination of circuit parameters

The resistance R_N of the normal channel was given by $R_N = R_0/f_N$, where R_0 is the K_3C_{60} thin film resistance, accounting for contact and wire resistance by subtracting the measured resistance far below T_c, and f_N is the fraction of normal carriers. We also

assume that $f_N + f_S = 1$, where f_S is the fraction of supercarriers. The kinetic inductance for each channel was determined in the same way, with the inductance of the normal channel given by $L_N = L_0/f_N$ and that of the superconducting channel given by $L_S = L_0/f_S$. The total kinetic inductance L_0 of the sample was estimated using equation (4.5). For the 20 μm × 20 μm × 100 nm thin film of K_3C_{60}, with a carrier density $n = 1.6 \times 10^{25}$ m^{-3}, as extracted from optical reflectivity measurements [12], $L_0 =$ 22 pH was obtained.

Circuit equations

The following circuit equations were derived from the two-fluid model:

$$2\Delta V = I_N R_N - V_0 + I_N \frac{dL_N}{dt} + L_N \frac{dI_N}{dt}, \tag{4.10}$$

$$I_S \frac{dL_S}{dt} + L_S \frac{dI_S}{dt} = I_N R_N + I_N \frac{dL_N}{dt} + L_N \frac{dI_N}{dt}, \tag{4.11}$$

$$I_{DC} - \frac{\Delta V}{Z_W} = I_N + I_S, \tag{4.12}$$

where V_0 is the initialised voltage across the sample, and other parameters are defined as displayed in Figure S21. These circuit equations were rearranged to the following form used for the numerical calculations:

$$\begin{aligned}\frac{d\Delta V}{dt} = \frac{Z_W(L_N + L_S)}{L_N L_S}\Bigg\{&-\left[2 + \frac{L_N}{Z_W(L_N + L_S)}\frac{dL_S}{dt}\right]\Delta V \\ &+ \left[R_N + \frac{dL_N}{dt} - \frac{L_N}{L_N + L_S}\left(R_N + \frac{dL_N}{dt} + \frac{dL_S}{dt}\right)\right] I_N + \frac{I_{DC} L_N}{L_N + L_S}\frac{dL_S}{dt} \\ &- V_0\Bigg\},\end{aligned} \tag{4.13}$$

$$\frac{dI_N}{dt} = \frac{1}{L_N + L_S}\left[-\frac{L_S}{Z_W}\frac{d\Delta V}{dt} - \frac{1}{Z_W}\frac{dL_S}{dt}\Delta V - \left(R_N + \frac{dL_N}{dt} + \frac{dL_S}{dt}\right) I_N + I_{DC}\frac{dL_S}{dt}\right]. \tag{4.14}$$

The equations were solved numerically with a time-dependent quasiparticle density contributing to the 'normal' resistive carrier density f_N. The rise in quasiparticle density was assumed to follow a Rothwarf-Taylor profile[13]. The decay was assumed to be exponential in time.

S4.4. Granular two-fluid model

The full circuit model used for the granular two-fluid model simulations is displayed in Figure S22. The bias current and waveguide were modelled in the same way as in section S4.3.

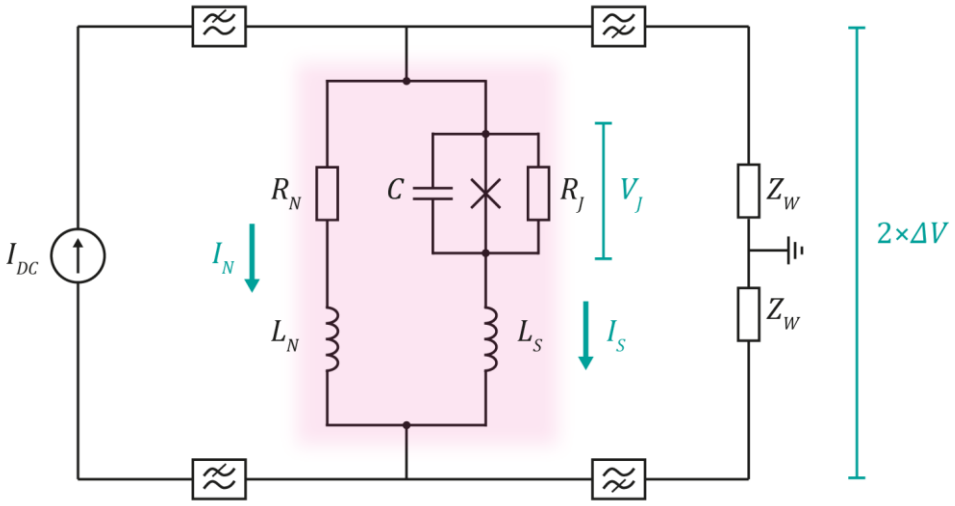

Figure S 22 | Full circuit model for granular two-fluid model simulations. The model for the sample is highlighted in red. The right part of the circuit represents the impedance of the coplanar waveguide.

Building upon the treatment discussed in Wang, *et al.* [2], the granular K_3C_{60} sample was modelled as an array of grains. From the atomic force microscopy measurement shown in Figure 1 of the main text, the grain size was 100 nm × 100 nm × 20 nm, meaning the full array for the 20 µm × 20 µm × 100 nm sample was a 200 × 200 × 5 structure of grains. We can write the number of grains in each direction as $N_L = 200$, $N_W = 200$, and $N_H = 5$, where N_L, N_W, and N_H represent the number of grains along the length, width, and height of the sample, respectively. The length is defined along the orientation parallel to the waveguide. The voltage changes across the length of the whole sample ΔV_{sample} could be related to the voltage changes across a single grain boundary ΔV_{grain} by

$$\Delta V_{grain} = \Delta V_{sample}/N_L\,. \tag{4.15}$$

Voltage changes across the whole sample could therefore be simulated by simulating the voltage changes across a single grain boundary.

Determination of circuit parameters

The resistance R_N of the normal channel was determined in the same way as outlined in section S4.3. The resistance at the grain boundary R_J for the superconducting state was given by $R_J = R_0/f_S$. For this model, resistances were scaled down to a single grain as $R \times (N_W \times N_H/N_L)$.

The kinetic inductances for each channel were also determined in the same way as in section S4.3, except inductances were scaled down to a single grain as $L \times (N_W \times N_H/N_L)$.

The capacitance for a single grain boundary C was estimated to be $C \approx 10^{-17}$ F, as discussed in Wang, *et al*. [2].

The critical current I_c of the Josephson junction was also considered to be proportional to the carrier density, following $I_c = I_c(T) \times f_S$. The temperature dependence of the critical current was given by $I_c(T) = I_c(0\ \mathrm{K})[1 - (T/T_c)^{1.5}]$ [14]. All currents, including the critical current, were also scaled down to a single grain as $I/(N_W \times N_H)$.

Finally, voltages were calculated for a single grain, and scaled up to the full sample as $V \times N_L$.

Circuit equations

The following circuit equations were derived from the granular two-fluid model:

$$2\Delta V = I_N R_N - V_0 + L_N \frac{dI_N}{dt} + I_N \frac{dL_N}{dt}, \tag{4.16}$$

$$I_N R_N + L_N \frac{dI_N}{dt} + I_N \frac{dL_N}{dt} = V_J + L_S \frac{dI_S}{dt} + I_S \frac{dL_S}{dt}, \tag{4.17}$$

and

$$I_{DC} - \frac{\Delta V}{Z_W} = I_N + I_S, \tag{4.18}$$

where V_0 is the initialised voltage across the sample, and other parameters are defined as displayed in Figure S22. The voltage V_J refers to the voltage drop across the resistively- and capacitively-shunted Josephson junction, and was governed by the following equations[15]:

$$\frac{dV_J}{dt} = \frac{1}{C}\left(I_S - I_C \sin\theta - \frac{\mathrm{V_J}}{\mathrm{R_J}} - \mathrm{i_n(t)}\right), \tag{4.19}$$

and

$$\frac{d\theta}{dt} = \frac{2eV_J}{\hbar}. \tag{4.20}$$

The current $i_n(t)$ represents the noise current associated with the thermal phase fluctuations. A white-noise frequency spectrum was used with a zero-mean Gaussian amplitude distribution. The full-width half-maximum of the amplitude distribution was determined by comparing the equations of motion for the Josephson phase with the Langevin equation, giving $\sqrt{2k_BT/R_J}$. The circuit equations were rearranged to the form used for the numerical calculation:

$$\begin{aligned}\frac{d\Delta V}{dt} = \frac{Z_W(L_N+L_S)}{L_N L_S}\Bigg\{&-\left[2 + \frac{L_N}{Z_W(L_N+L_S)}\frac{dL_S}{dt}\right]\Delta V \\ &+ \left[R_N + \frac{dL_N}{dt} - \frac{L_N}{L_N+L_S}\left(R_N + \frac{dL_N}{dt} + \frac{dL_S}{dt}\right)\right] I_N + \frac{I_{DC}L_N}{L_N+L_S}\frac{dL_S}{dt} \\ &+ \left(V_J - V_{J0} - V_0\right)\Bigg\},\end{aligned} \tag{4.21}$$

$$\frac{dI_N}{dt} = \frac{1}{L_N+L_S}\left[-\frac{L_S}{Z_W}\frac{d\Delta V}{dt} - \frac{1}{Z_W}\frac{dL_S}{dt}\Delta V - \left(R_N + \frac{dL_N}{dt} + \frac{dL_S}{dt}\right) I_N + I_{DC}\frac{dL_S}{dt}\right], \tag{4.22}$$

$$\frac{dV_J}{dt} = \frac{1}{C}\left[I_{DC} - \frac{\Delta V}{Z_W} - I_C \sin\theta - \frac{V_J}{R_J} - \mathrm{i_n(t)}\right], \tag{4.23}$$

$$\frac{d\theta}{dt} = \frac{2eV_J}{\hbar}. \tag{4.24}$$

The initial phase was randomised for each run, and the other variables were initialised based on the applied current and equilibrium sample properties. The simulation data were then convolved with the transmission spectrum of the waveguide (Figure S3a) and correlated with the time profile of the photo-conductive switch [2].

S4.5. Fitting of low-fluence excitation data below T_c

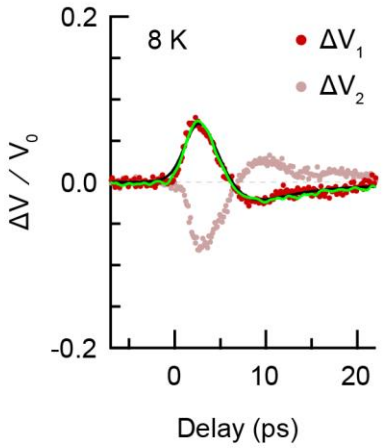

Figure S 23 | Two-fluid model fits to low-fluence data. The measured data from Figure 3b in the main text is shown in red/pink. The data is fitted with the simple two-fluid model (black line) and the granular two-fluid model (green line).

Figure S23 shows the two-fluid model fittings for the low-fluence excitation case with $T < T_c$, modelled using a Rothwarf-Taylor profile[16] for the rise of quasiparticle density, followed by an exponential decay. The simple two-fluid model fitting is discussed in the main text. For the granular two-fluid model fitting, we obtained a pair-breaking timescale $\tau_{PB} = 0.6 \pm 0.2$ ps and a recovery timescale $\tau_R = 30 \pm 5$ ps, which are comparable with the timescales obtained for the simple two-fluid model fit. In the low temperature limit, where thermally-induced phase slips have a negligible effect on transport and the sample displays zero resistance, the granular two-fluid model reproduces the behaviour of the simple two-fluid model and therefore also reproduces the data.

S5. Additional data

S5.1. Photo-excitation below T_c

S5.1.1. Photo-excitation above the critical current

A negative change in voltage drop was also observed upon photo-excitation of the K_3C_{60} thin film at temperatures below T_c, when the applied bias current was above the critical current of the equilibrium superconducting state. The time-resolved change in voltage for photo-excitation at 8 K under a 4-mA bias is displayed in Figure S24. A two-timescale voltage response was also observed under these conditions, similar to the voltage changes observed for the photo-induced state above T_c.

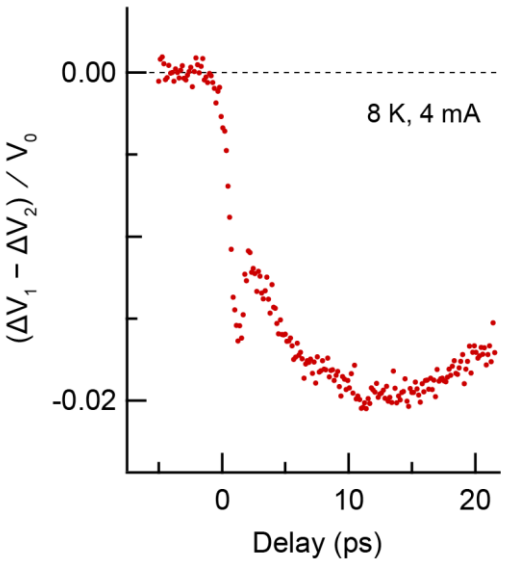

Figure S 24 | Photo-excitation above I_c. Normalised voltage changes versus pump-probe delay for photo-excitation at 8 K with an applied current of 4 mA (~$2I_c$). Data were taken with a fluence of 5 mJ/cm^2.

S5.2. Photo-excitation above T_c

S5.2.1. Fluence dependence

The fluence-dependent voltage changes for photo-excitation at 25 K are shown in Figure S25. At low fluences, the photo-induced voltage change had a shorter lifetime, and followed an exponential decay rather than the two-timescale behaviour observed at high fluences.

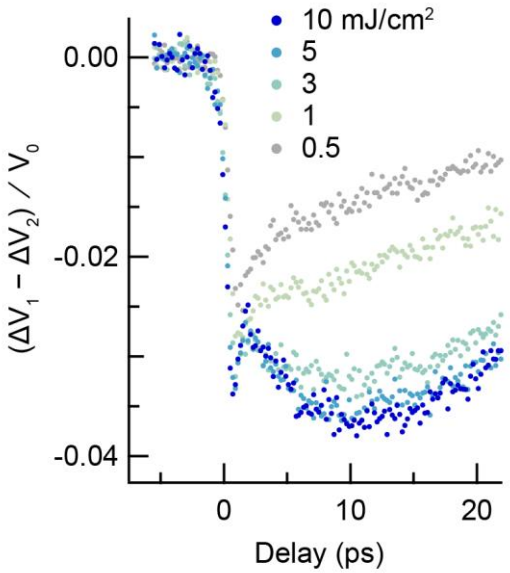

Figure S 25 | Fluence dependence for the photo-induced state above T_c. Normalised voltage changes versus pump-probe delay for photo-excitation at 25 K for mid-infrared excitation fluences of 0.5, 1, 3, 5, and 10 mJ/cm^2. Data were taken with applied current of 1 mA.

Upon increasing the fluence, the voltage changes increased in magnitude and the spike-and-dip structure emerged, saturating at approximately 5 mJ/cm^2.

S5.2.2. Current dependence vs fluence

Figure S26 displays the current dependence of the voltage changes at different fluences. Although the signal was reduced for smaller excitation fluence, a nonlinear current dependence was still observed at 1 mJ/cm^2.

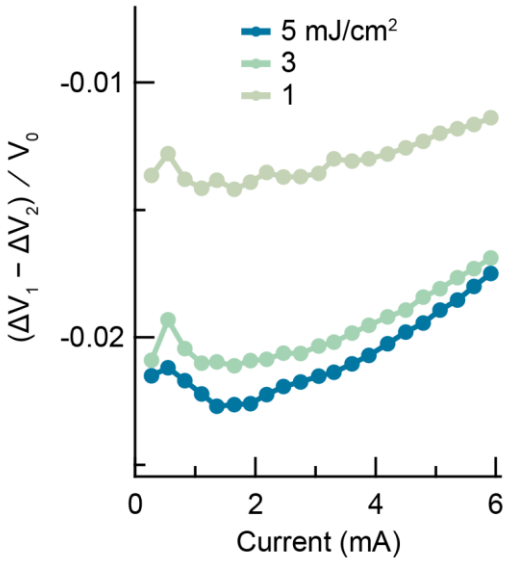

Figure S 26 | Fluence dependence of the nonlinear I-V behaviour. Normalised voltage changes versus current for photo-excitation at 25 K, with mid-infrared excitation fluences of 1, 3, and 5 mJ/cm^2.

References

1 Kozich, V., Moguilevski, A. & Heyne, K. High energy femtosecond OPA pumped by 1030nm Yb:KGW laser. *Optics Communications* **285**, 4515-4518 (2012).

2 Wang, E. *et al.* Superconducting nonlinear transport in optically driven high-temperature K_3C_{60}. *Nature Communications* **14**, 7233 (2023).

3 Degiorgi, L. *et al.* Optical properties of the alkali-metal-doped superconducting fullerenes: K_3C_{60} and Rb_3C_{60}. *Physical Review B* **49**, 7012-7025 (1994).

4 Klein, O., Grüner, G., Huang, S. M., Wiley, J. B. & Kaner, R. B. Electrical resistivity of K_3C_{60}. *Physical Review B* **46**, 11247-11249 (1992).

5 McIver, J. W. *et al.* Light-induced anomalous Hall effect in graphene. *Nat Phys* **16**, 38-41 (2020).

6 Meservey, R. & Tedrow, P. M. Measurements of the Kinetic Inductance of Superconducting Linear Structures. *Journal of Applied Physics* **40**, 2028-2034 (1969).

7 England, P., Venkatesan, T., Wu, X. D. & Inam, A. Granular superconductivity in $R_1Ba_2Cu_3O_{7-\delta}$ thin films. *Physical Review B* **38**, 7125-7128 (1988).

8 Abraham, D. W., Lobb, C. J., Tinkham, M. & Klapwijk, T. M. Resistive transition in two-dimensional arrays of superconducting weak links. *Physical Review B* **26**, 5268-5271 (1982).

9 Semenov, A. D., Nebosis, R. S., Gousev, Y. P., Heusinger, M. A. & Renk, K. F. Analysis of the nonequilibrium photoresponse of superconducting films to pulsed radiation by use of a two-temperature model. *Physical Review B* **52**, 581-581 (1995).

10 Sobolewski, R. Ultrafast dynamics of nonequilibrium quasi-particles in high-temperature superconductors. *SPIE* **3481**, 480-491 (1998).

11 Allen, K. & Hellman, F. Specific heat of C_{60} and K_3C_{60} thin films for T=6—400 K. *Physical Review B* **60**, 11765-11772 (1999).

12 Mitrano, M. *et al.* Possible light-induced superconductivity in K_3C_{60} at high temperature. *Nature* **530**, 461-464 (2016).

13 Mitrano, M. *Nonequilibrium emergent phenomena in organic molecular solids* PhD thesis, University of Hamburg, (2015).

14 Tinkham, M. *Introduction to Superconductivity, 2nd Edition*. (Dover Publications, Inc., 2004).

15 Ambegaokar, V. & Halperin, B. I. Voltage Due to Thermal Noise in the DC Josephson Effect. *Physical Review Letters* **22**, 1364-1366 (1969).

16 Rothwarf, A. & Taylor, B. N. Measurement of Recombination Lifetimes in Superconductors. *Physical Review Letters* **19**, 27-30 (1967).